Counterwind Currents in the China Shelf Seas: The Origin of the Pressure Gradient Driver

WEICONG CHENG[a] AND JIANPING GAN[a]

[a] *Center for Ocean Research in Hong Kong and Macau, Department of Ocean Science and Department of Mathematics, Hong Kong University of Science and Technology, Hong Kong, China*

(Manuscript received 28 January 2025, in final form 4 October 2025, accepted 7 November 2025)

ABSTRACT: There exist unique northeastward counterwind currents (CWCs) over the China shelf seas, subject to the balance between the northeastward alongshore ageostrophic (effective) pressure gradient force (PGF^{eff}, the residual PGF after balancing the Coriolis force) and southwestward surface wind stress forcing. The underlying physics for the formation of the alongshore PGF remains largely ambiguous. We used process-oriented modeling of the China shelf seas to investigate how the alongshore PGF and subsequent CWC form. Driven by a typical alongshore variable density field and wind forcing, our numerical model produced a realistic shelf current structure and CWC. Our results show that the alongshore sea level elevation gradient, induced by an alongshore variable wind, mainly contributed to the PGF, which is consistent with arrested topographic wave theory. However, the wind-induced elevation gradient alone is insufficient to overcome the frictional effects of wind forcing to form the CWC. The alongshore density gradient, due to heterogeneous heating, enhances the PGF because of the steric effect on sea level. The enhanced PGF produced by the density gradient and wind-induced elevation gradient critically forms the CWC. In addition, the seasonally variable density gradient and wind forcing determine the spatiotemporal variability of the CWC. We found that the dominant intrinsic dynamics of the wind and buoyancy forcing are enough to trigger the CWCs, and the shelf's topographic features further shape the structure of the CWC. The study provides new insights into the formation of CWC, which has been widely observed over the shelves globally.

KEYWORDS: Coastal flows; Continental forcing; Pressure; Topographic effects; Wind stress

1. Introduction

We present a dynamic analysis of counterwind currents (CWCs) in the China shelf seas. Cheng and Gan (2025, manuscript submitted to *J. Geophys. Res. Oceans*) used a realistic simulation based on the China Sea Multiscale Modeling System (CMOMS; https://odmp.hkust.edu.hk/cmoms/; Gan et al. 2016) to identify that the alongshore ageostrophic acceleration, followed by a cross-shore geostrophic adjustment, induced temporal variations of the CWCs during downwelling favorable wind seasons (referred to as downwelling seasons for short, hereafter). Cheng and Gan (2025, manuscript submitted to *J. Geophys. Res. Oceans*) found that the alongshore ageostrophic forcing ($FORCE_{x^*}$, where x^* denotes the alongshore direction) was provided by the pressure gradient force (PGF) and partly offset by Coriolis (COR) force and surface wind stress (SSTR). The spatially variable ageostrophic balance generates the alongshore varying characteristics of the shelf currents.

These alongshore PGF-induced CWCs have been observed in other regions around the world. For example, the depth-averaged CWC along the westward Middle Atlantic Bight shelf flow is primarily driven by an along-shelf PGF, countering the wind-driven eastward flow (Lentz 2008; Xu and Oey 2011). Xu and Oey (2011) found that it was fresh river water and the coastal Labrador Sea Water transport that produced the along-shelf PGF off the North American Pacific coast. Connolly et al. (2014) found that barotropic and baroclinic alongshore PGF, responding to a coastal trapped wave (CTW), drives the counterwind California Undercurrent. Furthermore, the alongshore PGF in the upwind direction could force a northward current over the continental shelf off Northern California when the wind relaxed (Gan and Allen 2002). The principal mechanism producing the poleward counterwind Leeuwin Current is thought to be the alongshore PGF formed by the steric effect on sea level (Godfrey and Ridgway 1985; McCreary et al. 1986; Morrow and Birol 1998). A common thread among most of these studies, however, was that none explicitly provided a holistic analysis of the dynamics of a CWC over a shelf that had complex topography and variable wind-driven circulation.

It is conceivable that the PGF drives these CWCs, but what dynamic process causes the alongshore PGF to form? In the South China Sea, it is the large-scale northeastward downward tilting sea level from the northern South China Sea (NSCS) to the East China Sea (ECS) (Fang and Zhao 1988; Zhai et al. 1993; Zhang 2002) that is considered to be the driving force of the CWC system for the region (Fang et al. 1991). Fang and Zhao (1988) suggested that the high sea level elevation in the western tropical Pacific and relatively low elevation in the northwest Pacific lead to the elevation gradient in the China shelf seas, and Zhang (2002) suggested that the tilt is associated with the subsurface density structure, atmospheric forcing, wave breaking, and the coastal currents caused by the flow interacting with topography. However, detailed dynamic analyses are still lacking despite a recent study by Lin et al. (2021) suggesting that the elevation tilt along the coast of China shelf seas during downwelling seasons could be predicted by the arrested topographic wave (ATW) theory (Csanady 1978).

Denotes content that is immediately available upon publication as open access.

Corresponding author: Jianping Gan, magan@ust.hk

DOI: 10.1175/JPO-D-25-0023.1

In addition, on a smaller scale, the blocking effect of topography, which occurs at Hainan Island (HNI) (Hong and Wang 2006; Zeng et al. 1989), in the Gulf of Tonkin (Chiang et al. 2008), and over Taiwan Bank (TWB) (Li et al. 2018; Shen et al. 2019), is considered to be important to the alongshore elevation tilt in the NSCS and Taiwan Strait (TWS). In these topographic cases, researchers have suggested that the southwestward wind stress drives the downwind current, leading to a high sea level elevation because of water mass accumulation caused by the topographic features. When the wind forcing relaxes, the elevation gradient generates the CWC (Guan and Fang 2006; Shen et al. 2019; Yu et al. 2021; Zhang et al. 2018). However, our current process-oriented study shows that intrinsic dynamics associated with the wind forcing set up the PGF to produce the CWC, and the influence of the topography is limited.

In addition to forcing within the NSCS, external forcing from the Kuroshio intrusion contributes to the CWC when the Kuroshio's mainstream passes Taiwan Island. Yang (2007) suggested that the lateral friction sets up a pressure difference between the southern and the northern tips of southeastern Taiwan Island, which is also felt on the other side of the island, and sustains the CWC. Wang et al. (2011) proposed that the Kuroshio intrusion is responsible for the PGF over the eastern part of the NSCS, and wind-induced Ekman pumping mainly contributes to the PGF on the western segment. Chuang (1985) argued that the Kuroshio intrusion on the southwestern side of Taiwan raises the sea level at the southern end of the Taiwan Strait relative to the northern end. Nonetheless, all these studies ignored the effects of wind-driven intrinsic dynamics over the shelf.

We see that due to the complex topography and varying dynamic forcing of the China shelf seas, how the PGF is generated remains unclear. Knowing what determines the PGF is essential to understand the dynamics of the CWC. In this study, we configured a process-oriented idealized model to isolate the contributions to the alongshore PGF from different processes to understand how the CWC forms.

2. Model configuration

We used the Regional Ocean Modeling System (ROMS model) to develop our process-oriented idealized model (Shchepetkin and McWilliams 2005). Our model adopted an idealized geometry that preserved the spatial scale and characteristics of the China shelf seas from the NSCS to ECS (box surrounded by black lines in Fig. 1a) to isolate the physical processes and identify the driving forces of the CWC dynamics. These underlying dynamics would be difficult to identify in a more complex, realistic model. The shoreward boundary of the idealized model aligned with the coastline of mainland China. The western boundary of the domain was west of Hainan Island. The domain extended northward to 33°N to cover the CWCs in the ECS. The western and northern boundaries extended far enough with a sponge zone (partly shown by the gray shading in Fig. 2a) to avoid the influence of the open boundary conditions. We defined the nearshore part (water depth, h, <100 m) in the sponge zone to be the closed boundary (blue patches in Fig. 2a) to mimic the semienclosed China shelf seas (Fig. 1). We defined the maximum water depth to be 400 m. We used the radiation boundary condition for the deeper part ($h > 100$ m) of the lateral boundaries and the open sea boundary.

We designed numerical experiments with different configurations to determine the fundamental dynamics that generate the CWC (listed in Table 1). Wind forcing and density variations (due to the meridional variations in air–sea heat transport) dominate the seasonal sea level variations along the coast of the China shelf seas (Feng et al. 2015; Lin et al. 2021; Qu et al. 2022). Therefore, we incorporated these two factors into our idealized model. We conducted three baseline case studies to quantify the contributions of the alongshore variable density (by specifying the alongshore variation initial field but not any external buoyancy forcing) and wind forcing to the alongshore tilting elevation under winter conditions, noting that CWCs exist under the strongest northeasterly winds. The three case studies were 1) case D, with alongshore variable initial density field but no wind forcing; 2) case W, with alongshore variable wind forcing and a horizontally uniform initial density field (with uniform vertical stratification, $N^2 = 5 \times 10^{-5}$ s^{-2}, the stratification is weak and has a small contribution to the thermal wind balance under the downwelling circulation); and 3) case DW, with simultaneous alongshore variable initial density field and wind forcing. To resolve the temporal variations of the China shelf seas, two seasonal variation cases adopted the initial alongshore variable density and wind forcing conditions for spring and autumn: case DW_spr and case DW_aut, respectively. We compared the results of the seasonal cases to case DW to highlight the temporal characteristics of the CWC. We configured a uniform cross-shore sloping shelf topography (Fig. 2b) without alongshore variation for the above cases to avoid the influence of the topography on our baseline and seasonal results. However, we did evaluate the contributions of different topographic features (yellow shading and red contour lines in Fig. 2a) of the China shelf seas in four topographic cases (Table 1) based on case DW, which we introduce in section 2c. Table 1 lists the configurations for all the numerical experiments.

a. Initial field

We obtained the typical seasonally averaged initial density field and wind forcing from CMOMS (Gan et al. 2016). Figures 3a–c show the alongshore density structure along the 400-m isobath (red line in Fig. 1a) from the continental slope close to the China shelf seas. The alongshore density structure had similar characteristics in different seasons, with northward increasing density and a pycnocline between 20- and 60-m depths, while the vertical density gradient was weak above 20-m and below 60-m depth. For simplicity, but including the essential characteristics in the density structure over the China shelf seas, we configured the initial vertical density profile with the following equation:

$$\rho(z) = \left(\rho^s + \frac{\rho^s - \rho_0^b}{h} z\right) + \frac{\Delta\rho_p}{2}\left[1 - \tanh\left(\frac{z - z_p^m}{0.5h_p}\right)\right], \qquad (1)$$

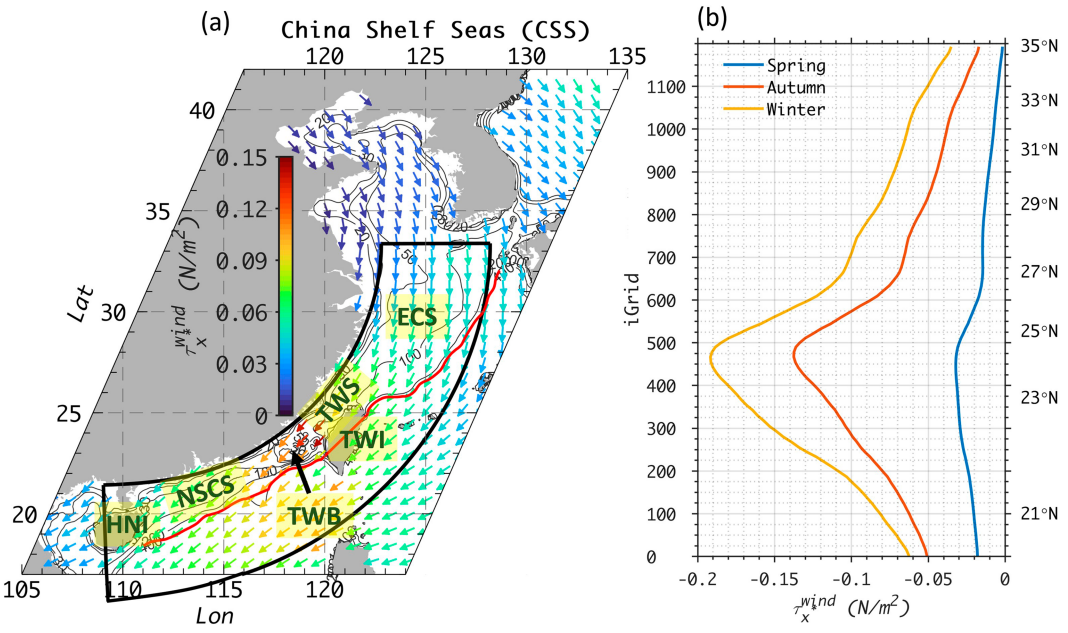

FIG. 1. (a) Wind stress vectors (arrows with color showing the magnitude) over the China shelf seas averaged over the downwelling seasons. The box depicted by black lines shows the focus domain of the process-oriented idealized model. The gray contour lines show the 20-, 50-, 100-, 200-, and 400-m isobaths. The red line highlights the selected 400-m isobath shown in Fig. 3. The black text boxes with yellow backgrounds identify the important locations: HNI, NSCS, TWB, TWS, TWI, and ECS. (b) Averaged alongshore wind stress magnitude over the shelf between the 20- and 100-m isobaths during different seasons, with left axis labels showing the alongshore grid number of the idealized model (refer Fig. 2) and right axis labels showing the latitudes. Negative values refer to a southwestward wind stress.

where z is the vertical location in the water column, with the negative direction meaning downward; h is the water depth; ρ^s is the density at the sea surface; $\rho_0^b = \rho^b - \Delta\rho_p$, where ρ^b is the density at the sea bottom; and $\Delta\rho_p$ is the density difference between the top and the bottom of the pycnocline, and thus, $[(\rho^s - \rho_0^b)/h]z$ sets up the background stratification intensity. The h_p is the thickness of the pycnocline, and z_p^m is the vertical location of the middle of the pycnocline. Equation (1) has two parts: The first part is the linear variation from the surface to the bottom, constructing the weak constant stratification over the whole water column. The second part constructs the pycnocline by setting $\rho_1 = 0$ and $\rho_2 = \Delta\rho_p$ in Eq. (1) of Kao et al. (1985). The alongshore variable parameters reconstructed the alongshore density structures for different seasons, which are displayed in Figs. 3d–f, and for which the essential characteristics of the realistic model were retained (Figs. 3a–c). We used the alongshore density structures in Figs. 3d–f to construct the initial density field by ensuring there was no cross-shore density gradient to avoid a cross-shore geostrophic contribution to the alongshore flow from the initial density field.

b. *Wind forcing*

During the downwelling seasons (spring, autumn, and winter, when CWCs exist), the wind blows parallel to the coastline over the China shelf seas and has small cross-shore variations (Fig. 1a). Therefore, we averaged the alongshore wind component in the cross-shore direction over the shelf area (between the coastline and 100-m isobath) to force the idealized model (Fig. 1b). Wind forcing for different seasons has similar alongshore variable patterns but differs dramatically in magnitudes, with the strongest wind intensity within the Taiwan Strait and weakening northward and southward. The intensity of the downwelling favorable wind is strongest in winter, followed by autumn, and is much weaker in spring. We interpolated the alongshore variable wind stress to the idealized model grid in the alongshore direction (uniform in the cross-shore direction and no cross-shore component to exclude the influence from the wind stress curl).

c. *Topographic features*

A broad shelf characterizes the bathymetry of the China shelf seas near the coast. In our study, the shelf is the area with $h < 100$ m. There is a slope with a sharply increasing depth further offshore (Fig. 1a). Many small-scale topographic features interact with the shelf circulation. We configured a uniform shelf in our baseline and seasonal cases (Table 1) to isolate the alongshore varying wind- and density-induced physics. We used a typical cross-shore section of the NSCS to construct the cross-shore bathymetry (Fig. 2b). Our cross-shore model bathymetry has a broad shelf of about 190 km and a steep slope offshore. We set the minimum and maximum water depth to be 10 and 400 m and defined the offshore side to have a flat bottom. Increasing the maximum depth did not change the conclusions of this study.

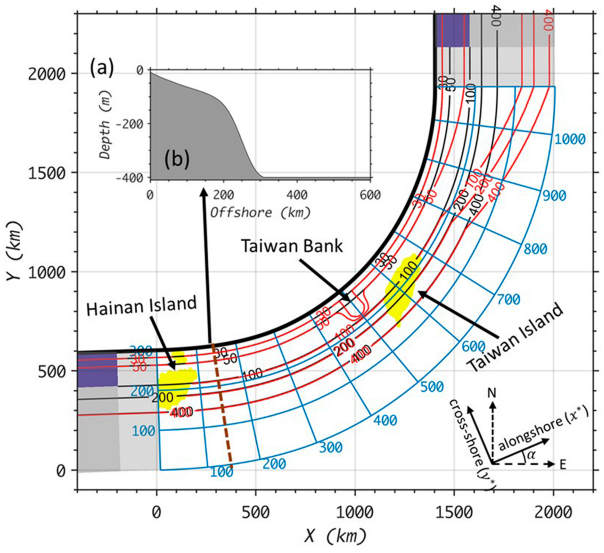

FIG. 2. Configurations of the idealized model. (a) The domain of the idealized model, with blue grid lines (every 100 grids) depicting the focus area. The light and dark gray shadings at the western and northern sides show the extended lateral boundary areas. The dark blue patches show the closed western and northern boundaries of the shelf. The blue contour lines show the bathymetry of the uniform shelf case. The red contour lines show the bathymetry with different topographies (including HNI, TWB, TWI, and the WS on the northern side). The thick black lines show the closed shoreward boundary. (b) The bathymetry of the cross-shore section [represented by the brown dashed line in (a)] in the case with the uniform shelf width. The alongshore and cross-shore directions are denoted in the bottom-right corner.

For the topographic cases (Table 1), we first investigated the influence of the widened shelf (WS) over the northern part of the ECS in case topo_S (north of 26°N, Fig. 1a). For this case, we increased the shelf width between the 30- and 100-m isobaths northeast of Taiwan Island to mimic the gradually widening ECS shelf (shown by red contour line in Fig. 2a). For case topo_SI, we added Taiwan Island according to its true location and size to determine the influence of the Taiwan Island (the yellow patch on the right in Fig. 2a), keeping the widened shelf. For Taiwan Bank (case topo_SIB), we conceptualized a shallow bank, with the shallowest depth equal to 20 m, located between the 30- and 100-m isobaths southwest of Taiwan Island. For case topo_SIBH, we used the case topo_SIB configuration and included Hainan Island (the yellow patch on the left in Fig. 2a).

3. Response of the CWC

In this section, we identify the response of the shelf circulation to the alongshore varying density and wind forcing using the results from the three baseline cases (case D, case W, and case DW). The figures in this paper are shown in alongshore (iGrid) and cross-shore (jGrid) grid number coordinates, which have 2–3-km resolution in the alongshore direction (increasing offshore) and constant 2-km resolution in the cross-shore direction. We defined northeast to be the positive alongshore direction (x^*) and shoreward as the positive cross-shore direction (y^*) (shown in the bottom-right corner in Fig. 2). The angle between the alongshore direction and geophysical eastward (α in Fig. 2) varied with the coastline's orientation, and we kept the local alongshore and cross-shore directions following the grid lines (blue lines in Fig. 2a). Accordingly, u^* and v^* are the alongshore and cross-shore velocities, respectively. We analyzed the average results from days 16 to 20, when the model reached a relatively steady state in all cases.

a. Horizontal response

Figure 4 shows the horizontal distribution of the sea level elevation and depth-mean currents over the shelf for the three baseline cases (case D, case W, and case DW). There was a negative alongshore elevation gradient (η_{x^*}) over the entire shelf in case D (Fig. 4a, with alongshore varying density), which formed a positive alongshore PGF (PGF_{x^*}). The alongshore varying wind also induced negative η_{x^*} in case W (Fig. 4b) with a stronger magnitude than in case D.

A positive (northward) depth-mean alongshore velocity (u^*) formed in case D over the entire shelf area, with larger magnitudes on the southwestern and offshore shelves, which were consistent with the cross-shore elevation gradient (η_{y^*}), indicating the alongshore flow was in geostrophic balance. For case W (Fig. 4b), the maximum elevation and negative

TABLE 1. Configurations of the numerical experiments.

Experiments	Initial field	Wind forcing	WS	TWI	TWB	HNI
		Baseline cases				
Case D	Winter	No wind				
Case W	Constant stratification	Winter				
Case DW	Winter	Winter				
		Seasonal variations				
Case DW_spr	Spring	Spring				
Case DW_aut	Autumn	Autumn				
		Topographical features				
Case topo_S	Winter	Winter	✓			
Case topo_SI	Winter	Winter	✓	✓		
Case topo_SIB	Winter	Winter	✓	✓	✓	
Case topo_SIBH	Winter	Winter	✓	✓	✓	✓

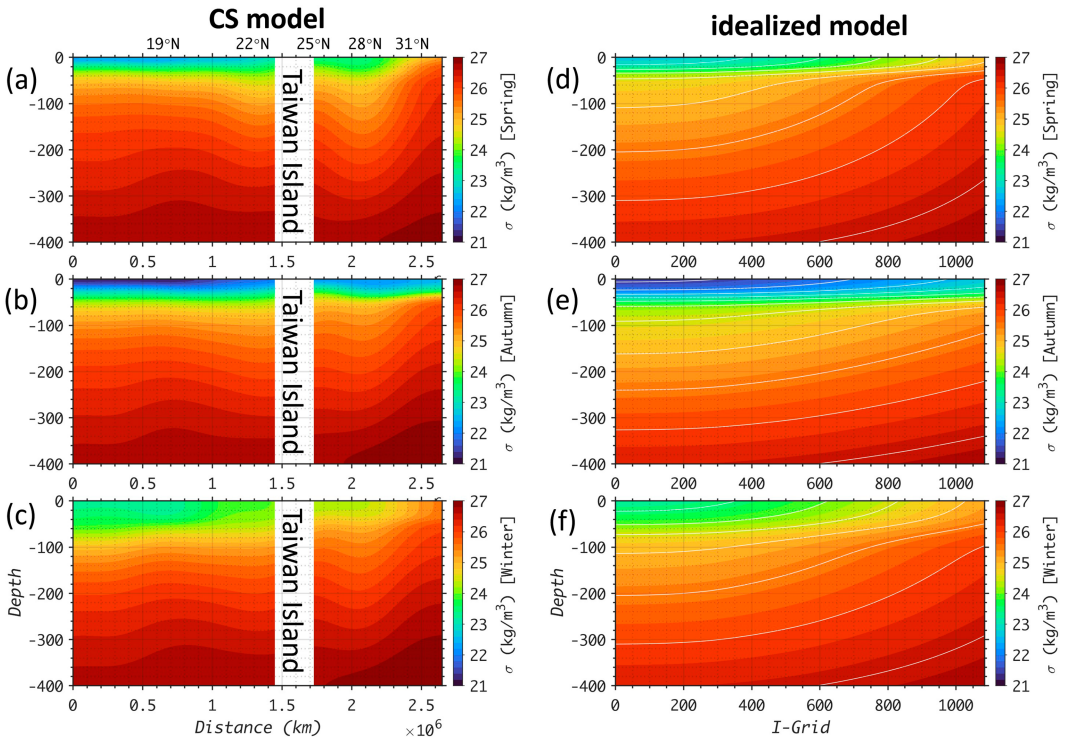

FIG. 3. Seasonally averaged density along the 400-m isobath (red line in Fig. 1) from the CMOMS in (a) spring, (b) autumn, and (c) winter. The initial density fields used in the idealized model are shown in (d) spring, (e) autumn, and (f) winter cases.

velocity were at iGrid = 300, which was at the southern side (in the propagation direction of the coastal trapped wave) of the maximum wind stress at iGrid = 490 (winter wind forcing shown the yellow line in Fig. 1b), indicating the nonlocal effect on the shelf dynamics (wind-induced ATW over the sloping topography; see section 4). The wind forcing set up a positive PGF_{x^*}. However, the positive PGF_{x^*} was not strong enough to overcome the negative wind stress (comparing $PGF^{w}_{x^*}$ and $SSTR_{x^*}$ in Fig. 7a); thus, the alongshore flow was in the downwind direction. The intensity of the downwind alongshore flow was stronger in the southern part than in the northern part in response to the alongshore variable wind forcing.

For case DW (Fig. 4c), the negative η_{x^*} was stronger than in case D and case W, indicating the combined effects of the alongshore variable density and wind forcing. However, the elevation did not decrease monotonically offshore. The elevation was the least along the 50-m isobath north of iGrid = 500, generating the negative η_{y^*} (favoring the positive u^*) over the outer shelf (between 50- and 100-m isobath).

The characteristics of the depth-mean currents also showed the joint influence of the two forces. On the shoreside of the 50-m isobath, the negative u^* was smaller for case DW compared to case W due to the density enhancing the positive PGF_{x^*}. On the seaward side of the 50-m isobath, the alongshore flow gradually turned to the counterwind direction from the southern shelf to the northern shelf, starting from iGrid = 250. Overall, the alongshore variable shelf currents in case DW were similar to the characteristics identified from the realistic China Seas model (Cheng and Gan 2025, manuscript submitted to *J. Geophys. Res. Oceans*) in which that CWC formed in Taiwan Strait and the ECS between the 50- and 100-m isobaths during winter, indicating that the alongshore varying density and wind forcing contributed to the formation and spatial characteristics of the CWCs. We discuss the related processes and mechanisms in sections 3c and 4.

b. *Vertical response*

Figure 5 shows the alongshore velocity (u^*) at the cross-shore section at iGrid = 500, where the magnitude of the alongshore wind stress was the strongest. For all three baseline cases (case D, case W, and case DW), the alongshore flow had a uniform direction but differed vertically in magnitudes.

For case D (Fig. 5a), there was a relatively uniform positive u^* (northward alongshore current) over the cross-shore section. For case W (Fig. 5b), stronger negative u^* was over the shallower water column because the wind was more important in the depth-mean momentum balance ($\tau^{\text{wind}}_{x^*}/h$, with uniform wind stress in the cross-shore direction). Larger negative velocity near the surface also indicated the direct effect of wind friction.

For case DW, the structure of u^* showed the combined effects of the alongshore varying density and wind forcing (comparing Fig. 5c with Figs. 5a,b). On the shoreside of the 60-m isobath, the wind-driven current dominated, and the intensity of the negative u^* was slightly weaker than in case W because it was partly offset by the density-driven positive u^*. On the

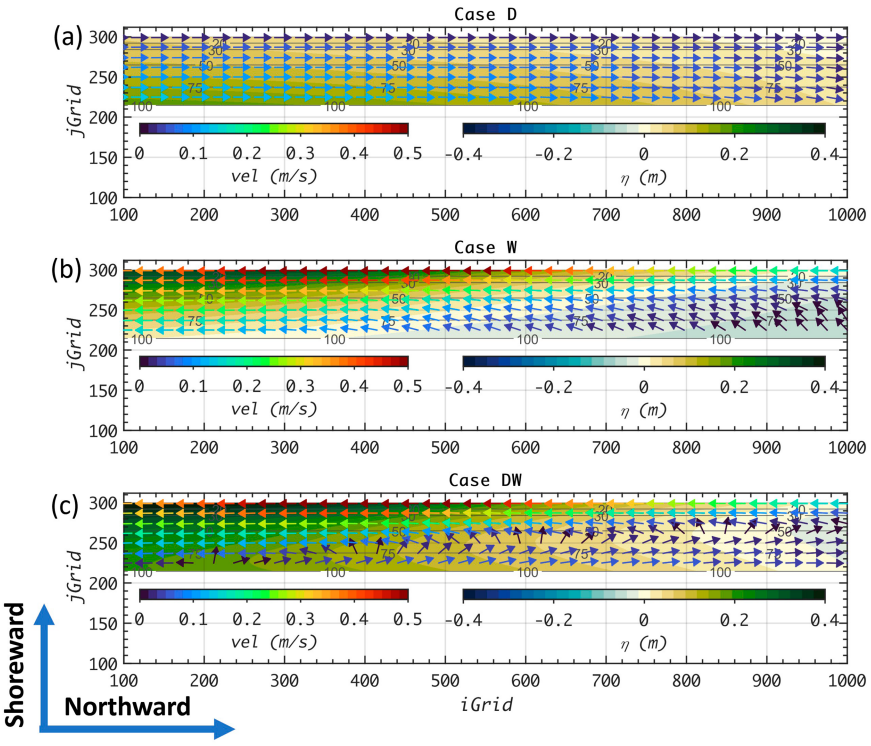

FIG. 4. Horizontal distribution of depth-mean velocity vectors (arrows with color showing the magnitude) and elevation (background colored shading) in (a) case D, with alongshore varying initial density; (b) case W, with alongshore varying wind forcing; and (c) case DW, with alongshore varying initial density and wind forcing. We averaged the results from day 16 to day 20. Each grid point is equivalent to 2 km in the cross-shore direction and 2–3 km (increasing seaward) in the alongshore direction. We adjusted the elevation to be zero at iGrid = 1000 and jGrid = 300 in each case.

offshore side of the 60-m isobath, the alongshore varying density effect contributed to the existence of the CWC. The intensity of the CWC weakened near the surface due to the effect of wind friction.

Overall, the wind forcing drove the southward downwind current over the whole shelf area (Fig. 5b) because the wind-induced alongshore elevation gradient could not overcome the frictional effect. Including the effect of the alongshore variable density in the scenario meant that the current direction reversed over the outer shelf (Fig. 5c). The direction of the shelf currents, including the CWC, was relatively uniform in the vertical direction with small variations in intensity.

c. *Formation of the CWC*

Because the alongshore flow direction had depth-independent characteristics (Fig. 5c), the dynamics behind CWC formation can be understood by the depth-mean alongshore momentum balance:

$$\overbrace{\frac{\partial u^*}{\partial t}}^{\mathrm{ACCEL}_{x^*}} = \overbrace{-\frac{1}{\rho_0}\frac{\partial P}{\partial x^*}}^{\mathrm{PGF}_{x^*}} \overbrace{+ fv^*}^{\mathrm{COR}_{x^*}} \overbrace{- u^*\frac{\partial u^*}{\partial x^*} - v^*\frac{\partial u^*}{\partial y^*}}^{\mathrm{HADV}_{x^*}} + \overbrace{\frac{\tau_{x^*}^{\mathrm{wind}}}{\rho_0 H}}^{\mathrm{SSTR}_{x^*}} + \overbrace{\frac{\tau_{x^*}^{\mathrm{bottom}}}{\rho_0 H}}^{\mathrm{BSTR}_{x^*}}, \quad (2)$$

where x^* denotes the alongshore direction, ACCEL_{x^*} is the acceleration term, PGF_{x^*} is the pressure gradient force term, COR_{x^*} is the Coriolis force term, HADV_{x^*} is the nonlinear horizontal advection term, SSTR_{x^*} is the surface wind stress term, and BSTR_{x^*} is the bottom stress term.

The spatially variable dynamic balance contributed to the variable shelf currents in case DW. Figure 6 displays the time series of the momentum terms and alongshore velocity at various locations to illustrate the key dynamic control of the formation of CWCs. We see that CWCs formed over the outer shelf of the middle and northern parts of the domain. Over the outer northern shelf (at the 75-m isobath along iGrid = 800, Fig. 6b), there was a quick setup of positive PGF_{x^*} that overcame the negative SSTR_{x^*} and generated the positive alongshore velocity, which was sustained by PGF_{x^*} and COR_{x^*}. Over the inner northern shelf (at the 30-m isobath along iGrid = 800, Fig. 6a), there was a stronger positive PGF_{x^*} setup compared to the outer shelf (Fig. 6b). However, the intensified negative SSTR_{x^*} ($\tau_{x^*}^{\mathrm{wind}}/h$) overcame PGF_{x^*} due to the shallow water, thus forming the negative velocity. The situations were similar over the entire inner shelf. Furthermore, CWCs did not form over the outer shelf in the south (Fig. 6c, at the 75-m isobath along iGrid = 300) because there was stronger negative wind stress compared to the north (Fig. 1b).

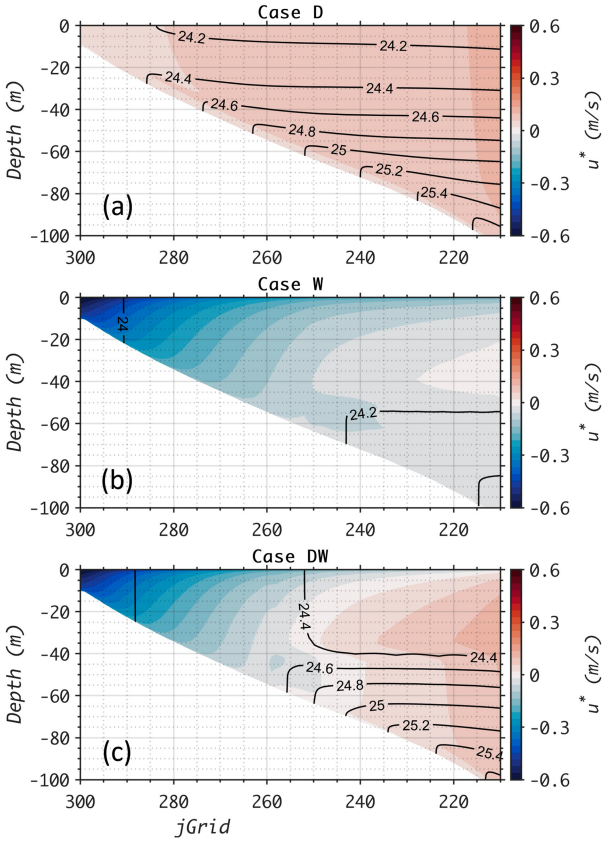

FIG. 5. Alongshore velocity (colored shading) and density (σ_t, contour lines) of the cross-shore section along iGrid = 500 of (a) case D, with alongshore varying initial density; (b) case W, with alongshore varying wind forcing; and (c) case DW with alongshore varying initial density and wind forcing. We averaged the results from day 16 to day 20.

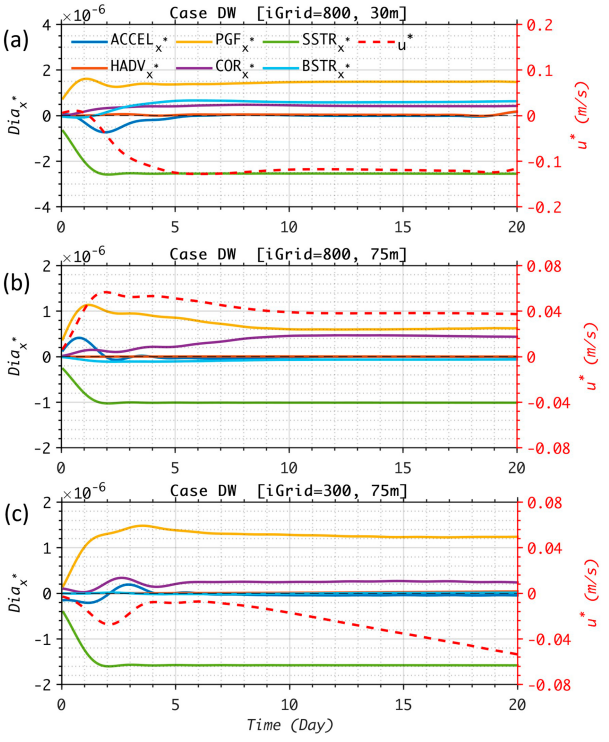

FIG. 6. Time series of the diagnostic depth-mean alongshore momentum terms (left axis) and depth-mean alongshore velocity (right axis) at the (a) 30-m isobath along iGrid = 800, (b) 75-m isobath along iGrid = 800, and (c) 75-m isobath along iGrid = 300 for case DW (refer to Figs. 2 and 4 for the locations).

The positive PGF_{x^*} was not enough to overcome the negative SSTR_{x^*}, and CWCs could not form.

Overall, Fig. 6 shows that the alongshore momentum balance was between SSTR_{x^*}, BSTR_{x^*}, PGF_{x^*}, and COR_{x^*}. The direction of u^* was determined by the sum of SSTR_{x^*}, PGF_{x^*}, and COR_{x^*} (denoted as FORCE_{x^*}). Due to the dominant contribution of SSTR_{x^*} over shallow water, CWCs could not form over the inner shelf. Therefore, we focused on the outer shelf (between 50- and 100-m isobaths), where the CWCs existed, to further investigate the dynamics of CWC formation.

Figure 7a displays the alongshore variations of the components of FORCE_{x^*} over the outer shelf for case DW. The FORCE_{x^*} was negative/positive to the south/north of iGrid = 600. The alongshore variations of FORCE_{x^*} were consistent with the depth-mean flow pattern (direction of u^*) shown in Fig. 4c, in which the flow was southward in the south, and the CWC gradually developed over the middle and northern parts of the outer shelf. Over most of the shelf, the magnitude of FORCE_{x^*} was between the balance of the negative SSTR_{x^*} and the positive PGF_{x^*} and COR_{x^*}, where PGF_{x^*} was the more important term, providing the potential forcing for the positive FORCE_{x^*} and CWC. The magnitude of COR_{x^*} varied with SSTR_{x^*}, indicating the downwelling wind-induced onshore transport offsets the frictional effect of the wind in the alongshore momentum balance. Therefore, we consider the sum of COR_{x^*} and SSTR_{x^*} to be the direct wind effect.

In summary, we found that positive PGF_{x^*} was the most important potential forcing that produces the CWCs over the outer shelf, and it was the elevation-slope-induced barotropic component that mainly contributed to the positive PGF_{x^*} (indicated by Fig. 8a). Negative $\tau_{x^*}^{\mathrm{wind}}$ was strongest at iGrid = 500, which should have led to the highest elevation at this location and generated a reversed elevation slope on its two sides according to Ekman theory. However, we found the highest elevation was in the southern part of the domain (Fig. 4c), and there was positive PGF_{x^*} (Fig. 7a) over the entire shelf, which meant that there must have been nonlocal dynamic processes that contributed to the alongshore elevation gradient (or PGF_{x^*}). We discuss the possibility in the discussion.

4. Discussion

a. *The alongshore pressure gradient force,* PGF_{x^*}

Figure 8a shows the alongshore variations of the total (solid lines) and baroclinic (dashed lines) PGF_{x^*} (averaged between the 50- and 100-m isobaths) of the three baseline winter cases

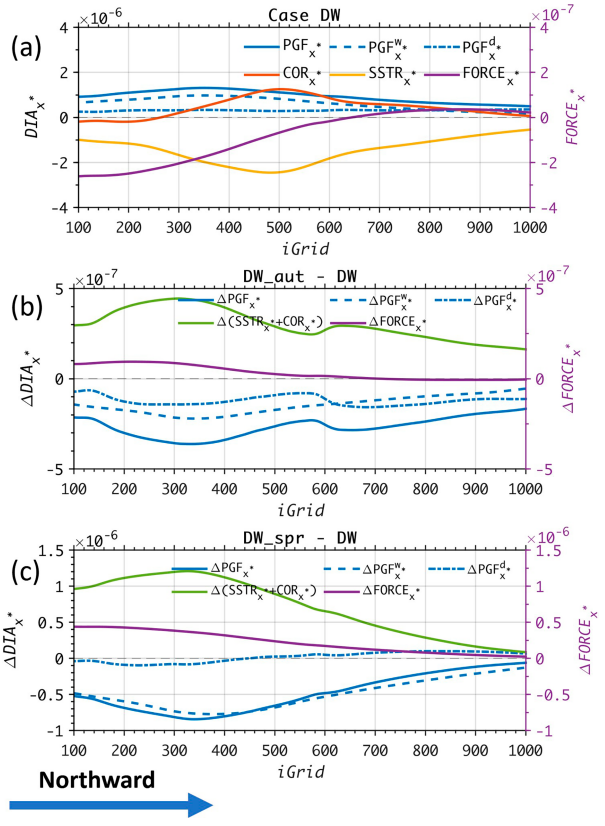

FIG. 7. Diagnostic depth-mean alongshore momentum terms averaged between the 50- and 100-m isobaths, including the PGF (PGF_{x^*}), COR force (COR_{x^*}), and SSTR ($SSTR_{x^*}$) (left axis) and the sum of the three terms ($FORCE_{x^*}$, right axis). The PGF_{x^*} is divided into the wind-induced ($PGF^{w}_{x^*}$) and density-induced ($PGF^{d}_{x^*}$) parts. (a) The momentum terms in case DW. (b) Difference of the terms between case DW_aut (forced by the alongshore varying density and wind forcing for autumn) and case DW. (c) Difference of the terms between case DW_spr (forced by the alongshore varying density and wind forcing for spring) and case DW. We averaged the model results in (a)–(c) from day 16 to day 20.

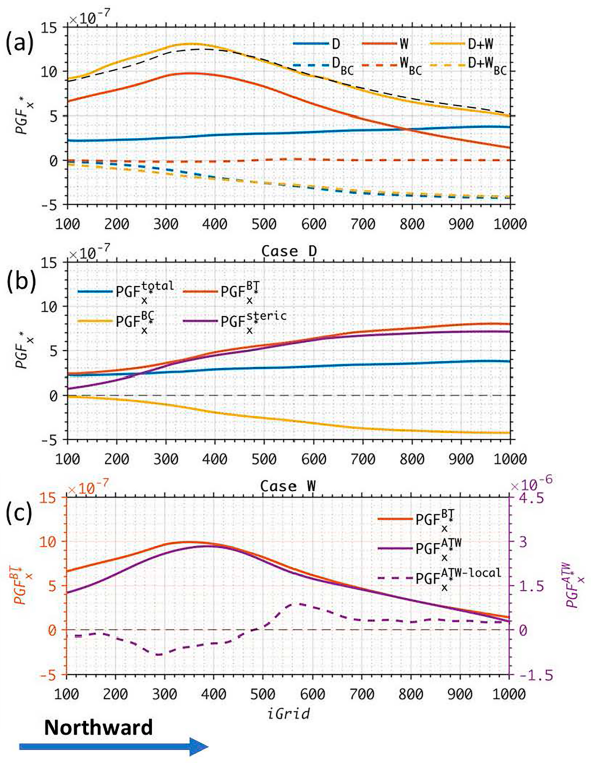

FIG. 8. Alongshore PGF (PGF_{x^*}) averaged between the 50- and 100-m isobaths. (a) The PGF_{x^*} from the three baseline cases (case D, case W, and case DW). The solid lines are the total PGF_{x^*} ($PGF^{total}_{x^*}$), and the dashed lines are the baroclinic components of PGF_{x^*} ($PGF^{BC}_{x^*}$). The black dashed line is the sum of $PGF^{total}_{x^*}$ for case D and case W. (b) Alongshore PGF_{x^*} from case D and the steric-induced $PGF^{steric}_{x^*}$ estimated from the initial field. (c) The $PGF^{BT}_{x^*}$ from case W (orange solid line, left axis), $PGF^{ATW}_{x^*}$ estimated from ATW theory (purple solid line, right axis), and the local solution of $PGF^{ATW}_{x^*}$ ($PGF^{ATW\text{-}local}_{x^*}$, dashed purple line, right axis). We averaged the model results in (a)–(c) from day 16 to day 20.

(case D, case W, and case DW). In case D, the baroclinic PGF_{x^*} (the blue dashed line) was negative due to the northeastward increasing density (Fig. 3f). The magnitude of the baroclinic PGF_{x^*} was larger in the northern part of the domain because of the stronger alongshore density gradient. However, we found the total PGF_{x^*} (the blue solid line) was positive over the shelf due to the dominant contribution from the barotropic component ($PGF^{BT}_{x^*}$ in Fig. 8b). The elevation slope setup for the barotropic PGF was related to the density-induced steric effect [section 4a(1)]. In case W, the baroclinic PGF_{x^*} (dashed orange line) was zero because of the uniform density in the horizontal direction (Table 1). The wind-induced η_{x^*} contributed to the total PGF_{x^*} (solid orange line). The magnitude of PGF_{x^*} was greatest at the southern (at iGrid = 350) side of the maximum wind stress (iGrid = 500), which was related to ATW dynamics [section 4a(2)].

For case DW, the alongshore variable density and wind forcing contributed to PGF_{x^*} almost linearly, indicated by the overlapping black dashed line (sum of the total PGF_{x^*} for case D and case W) and the solid yellow line (PGF_{x^*} for case DW). Therefore, PGF_{x^*} in case D (case W) could be considered as the density-induced contribution, $PGF^{d}_{x^*}$ (wind-induced contribution, $PGF^{w}_{x^*}$) for case DW (Fig. 7a). The alongshore PGF_{x^*} setup, contributed jointly by the alongshore variable density and wind forcing, overcame the direct wind effect and formed the CWCs in case DW.

1) STERIC EFFECT

The steric effect of sea level represents the vertical expansion or contraction of the water column due to the thermosteric and halosteric variations. Along the coast of the China shelf seas, the steric effect contributes to much of the seasonal variations of the sea level elevation (Feng et al. 2015; Qu et al. 2022) and leads to the alongshore elevation gradient over the shelf. Although ROMS is a Boussinesq numerical model, conserving the volume rather than the mass, the model adequately represents the steric sea effect caused by the gradient-

induced thermal wind balance (Greatbatch 1994; Laiz et al. 2014; Liu et al. 2016; Swapna et al. 2009).

To verify the steric effect of sea level, we calculated the steric sea level (η_s) following Gill (1982) according to the initial density structure (Fig. 3f):

$$\eta^s = -\frac{1}{\rho_0}\int_{-H}^{0}\rho' dz, \tag{3}$$

where ρ_0 is the reference density and $\rho' = \rho(S, T, p) - \rho(35, 0, p)$ is the density anomaly. We defined H to be 400 m in Eq. (2) to include the effect of deep water (Helland-Hansen 1934). The alongshore PGF_{x^*} due to the steric effect is defined by

$$\mathrm{PGF}_{x^*}^{\mathrm{steric}} = -g\frac{\partial \eta^s}{\partial x^*}. \tag{4}$$

Our results show that the magnitude and alongshore varying structure of $\mathrm{PGF}_{x^*}^{\mathrm{steric}}$ compared well to the barotropic component of PGF_{x^*} (or $\mathrm{PGF}_{x^*}^{\mathrm{BT}}$) from case D (with the alongshore variable density only, Fig. 8b). The intensity of the density-contributed $\mathrm{PGF}_{x^*}^{\mathrm{BT}}$ (or $\mathrm{PGF}_{x^*}^{\mathrm{steric}}$) was larger over the northern part of the domain due to the stronger horizontal temperature (density) gradient at the higher latitude during the winter and, thus, led to the larger $\mathrm{PGF}_{x^*}^{\mathrm{total}}$ in the northern part. The alongshore varying density-induced downward elevation tilt and alongshore current toward the denser water side in case D were consistent with density-modified ATW theory (Vennell and Malanotte-Rizzoli 1987).

2) Wind-induced arrested topographic wave

Lin et al. (2021) suggested that the wind-induced ATW over the sloping shelf sets up the alongshore elevation tilt along the coast of the China shelf seas, which also influences the shelf area away from the coast. Following Csanady (1978, 1981), and with the negative y^* to be the offshore direction and negative x^* to be the propagating direction of the coastal trapped wave, when wind stress is prescribed for $-X < x^* < 0$, then the ATW solution for the elevation (η^w) is

$$\eta^w = -\frac{\mathrm{A}_0 f F_0}{rg}\left((-Kx^*)^{1/2}\mathrm{erfc}\left[\frac{-y'}{2(-Kx^*)^{1/2}}\right] - [K(-X-x^*)]^{1/2}\mathrm{erfc}\left\{\frac{-y'}{2[K(-X-x^*)]^{1/2}}\right\}\right). \tag{5}$$

This solution is valid for $x^* \le -X$. For $-X \le x^* \le 0$, only the first term in the braces is present. In Eq. (4), A_0 is a constant, and we set $A_0 = 2$ following Csanady (1978, 1981). The F_0 is the wind stress, and g is the gravity acceleration. The f is the Coriolis parameter, which we set to the same value we used in the idealized model. The r is the linear drag coefficient with a value of 3×10^{-4} adopted. The $K = r/fs$, in which $s = 90$ m/180 km is the slope of the shelf. Because the ATW model is linear, solutions for different segments of constant wind stress can be added together to obtain the total predicted elevation at a given location (Hickey and Pola 1983). We calculated η^w by dividing the idealized model domain into 100 segments in the alongshore direction and averaging the wind stress of each segment. Then, we obtained the wind-induced PGF_{x^*} ($\mathrm{PGF}_{x^*}^{\mathrm{ATW}}$) like we did for Eq. (3).

Figure 8c compares $\mathrm{PGF}_{x^*}^{\mathrm{BT}}$ (orange solid line) from case W, $\mathrm{PGF}_{x^*}^{\mathrm{ATW}}$ calculated from ATW theory (purple solid line), and the estimated $\mathrm{PGF}_{x^*}^{\mathrm{ATW}}$ that only considered local Ekman dynamics [$\mathrm{PGF}_{x^*}^{\mathrm{ATW-local}}$, purple dashed line, only the first term in the braces from Eq. (4) is considered when calculating η^w]. The $\mathrm{PGF}_{x^*}^{\mathrm{BT}}$ and $\mathrm{PGF}_{x^*}^{\mathrm{ATW}}$ differed in magnitude but had similar alongshore structures. The difference could be because of assumptions in the ATW model, such as a linear bottom drag law, a constant slope of the topography, and zero elevation for the offshore boundary condition. Furthermore, Hickey and Pola (1983) set $A_0 = 1.12$ in Eq. (4) rather than $A_0 = 2$ from Csanady (1978, 1981), indicating that this parameter could vary and significantly influence the magnitudes of the elevation and elevation gradient. Still, the consistent alongshore structure demonstrated the importance of the ATW. When we only considered the local effect, $\mathrm{PGF}_{x^*}^{\mathrm{ATW-local}}$ was negative/positive south/north of iGrid = 500, which was consistent with the alongshore gradient of wind stress ($\partial\tau_{x^*}/\partial x^*$, indicated by Fig. 1b), and the magnitude of $\mathrm{PGF}_{x^*}^{\mathrm{ATW-local}}$ was much smaller than $\mathrm{PGF}_{x^*}^{\mathrm{ATW}}$. Therefore, we find that the nonlocal effect is important to CWC formation.

Overall, alongshore varying density and wind forcing contributed to the positive PGF_{x^*} over the shelf, which provided the potential forcing for the CWCs. The magnitudes of the barotropic PGF_{x^*} from these two effects were comparable (comparing $\mathrm{PGF}_{x^*}^{\mathrm{BT}}$ in Figs. 8b,c), with the stronger density (wind) contribution in the northern (southern) part of the shelf. However, the density-induced baroclinic effect offsets part of its barotropic component so that the total PGF_{x^*} induced by the density effect ($\mathrm{PGF}_{x^*}^{d}$) was smaller than the total induced by the wind ($\mathrm{PGF}_{x^*}^{w}$), except north of iGrid = 800 (Fig. 7a and more clearly shown by line D and line W in Fig. 8a). The wind setup $\mathrm{PGF}_{x^*}^{w}$ partly, but not entirely, offsets the negative SSTR_{x^*} and could not form CWCs (case W). The density effect was small but critical for the formation of CWCs (case DW).

b. *The seasonal variations*

We investigated the dynamics of the variabilities of CWCs in this section by configuring the idealized model for autumn (case DW_aut) and spring (case DW_spr) conditions with alongshore variable density and wind forcing.

The characteristics of the CWCs for case DW_aut were like the characteristics for case DW (comparing Fig. 9a with Fig. 4c). In both cases, the CWCs formed over the middle and northern parts of the domain (or the Taiwan Strait and ECS in the realistic China shelf seas). The characteristics of the CWCs were like those observed by satellites and observed in the realistic China Seas model results. The alongshore density gradient and wind stress were slightly smaller during the autumn than during the winter (comparing alongshore density distribution in Fig. 3e with Fig. 3f and wind forcing in Fig. 1b), contributing to the smaller positive $\mathrm{PGF}_{x^*}^{d}$ and $\mathrm{PGF}_{x^*}^{w}$ in case DW_aut compared to case DW (shown by the negative

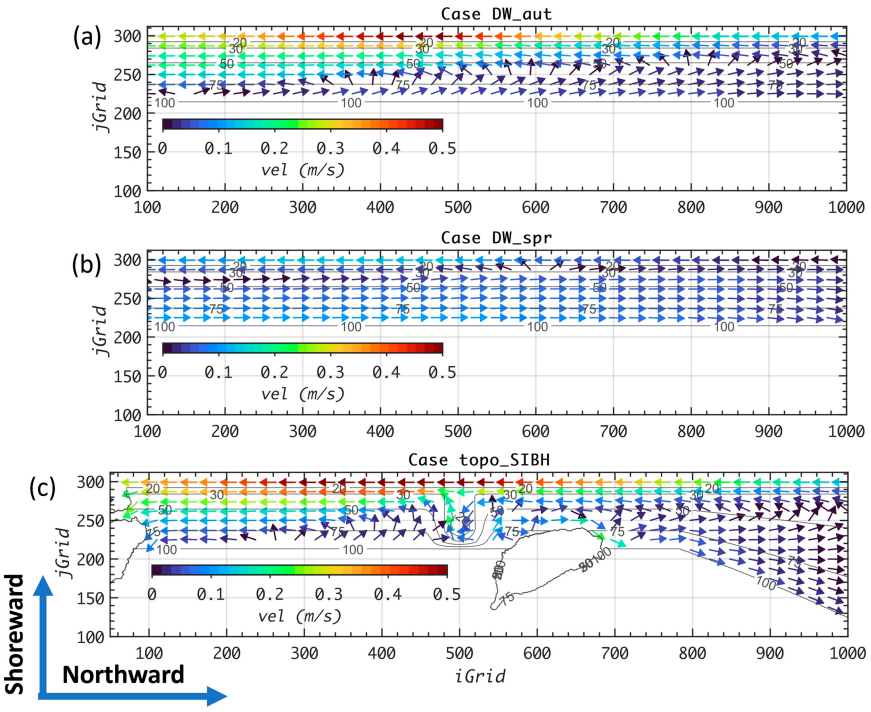

FIG. 9. Horizontal distribution of depth-mean velocity vectors (arrows with color showing the magnitude) in (a) case DW_aut, with alongshore varying initial density and wind forcing during autumn; (b) case DW_spr, with alongshore varying initial density and wind forcing during spring; and (c) case topo_SIBH, with alongshore varying initial density and wind forcing during winter and all the topographic features included (refer to Fig. 2). We averaged the results from day 16 to day 20.

$\Delta PGF^{d}_{x^*}$ and $\Delta PGF^{w}_{x^*}$ in Fig. 7b). At the same time, the intensity of the negative direct wind effect ($COR_{x^*} + SSTR_{x^*}$) weakened [positive $\Delta(COR_{x^*} + SSTR_{x^*})$ in Fig. 7b] and had a larger magnitude than PGF_{x^*} (sum of $\Delta PGF^{d}_{x^*}$ and $\Delta PGF^{w}_{x^*}$). Therefore, $\Delta FORCE_{x^*}$ was positive over the entire shelf, favoring the formation of CWCs, compared to winter conditions. As a result, the positive $FORCE_{x^*}$ extended southward to iGrid = 500 (not shown) and, thus, extended the coverage of the CWCs and enhanced the intensity slightly compared to the winter. Overall, the effects of a weakened southward wind forcing and decreased alongshore density gradient largely offset each other during autumn, producing autumn CWC characteristics like the winter CWC characteristics.

During spring (case DW_spr), the northeastward CWCs appeared in the entire outer shelf (Fig. 9b), and the CWCs extended shoreward in the northern part compared to winter (Fig. 4c). Again, the spatial characteristics of the CWCs were similar to those observed by satellites. The horizontal density gradients during the spring and winter (Figs. 3a,c) were similar, but the wind magnitude was much smaller during the spring (Fig. 1b). Therefore, the difference in the density-induced PGF_{x^*} ($\Delta PGF^{d}_{x^*}$ in Fig. 7c) between spring and winter was small. Larger differences occurred in wind-related terms. The negative direct wind effect weakened greatly [positive $\Delta(COR_{x^*} + SSTR_{x^*})$] especially in the southern part of the domain. The weakened wind stress also led to the smaller positive PGF_{x^*} during the spring (negative $\Delta PGF^{w}_{x^*}$ and ΔPGF_{x^*} in Fig. 7c). The overall effect was a positive $\Delta FORCE_{x^*}$ with a larger magnitude in the south, favoring the formation of the CWCs over the entire outer shelf. Therefore, during the spring, the weakened wind forcing mainly contributed to CWC formation in the southern part of the domain (or NSCS in the realistic China shelf seas).

c. *Effects of the topographic features*

The different topographic features of the China shelf seas, such as Hainan Island, Taiwan Island, and Taiwan Bank (Fig. 1), are considered important contributors to generating CWCs (see introduction). However, the roles of these topographic features are largely speculative and have not been dynamically validated. Figure 10 compares the alongshore variations of sea level elevation (Fig. 10a) and depth-mean alongshore velocity, u^* (Fig. 10b), of the cases considering different topographic features and all based on winter conditions. We averaged both parameters between the 50- and 100-m isobaths. We adjusted the elevations in all cases to be zero at iGrid = 1000 by subtracting a constant (different constants for each case) so that we could compare the elevation gradients, η_{x^*}, better.

1) WIDENED SHELF

The effects of the widened shelf in the ECS have not been discussed in historic studies. However, a narrowing (in the direction of the coastal trapped wave) shelf could modulate the

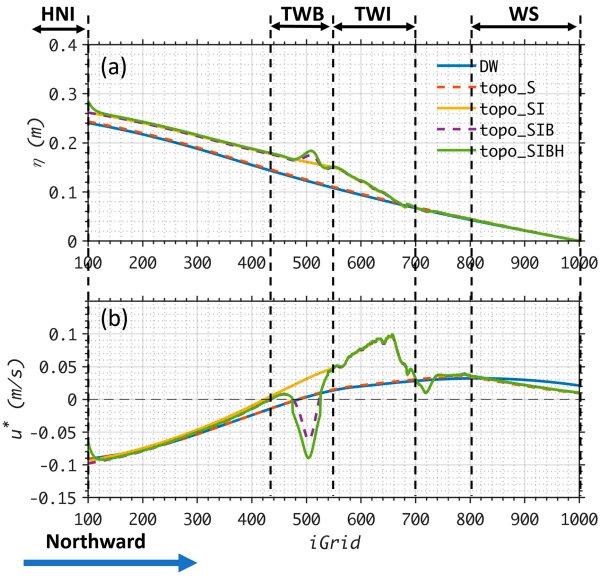

FIG. 10. (a) Alongshore elevation and (b) depth-mean alongshore velocity from the topographic cases (refer to Table 1 for details). We adjusted the elevations from (a) all cases to have zero elevation at iGrid = 1000 to compare the elevation gradients. The vertical dashed lines and labels denote the locations of HNI, TWB, TWI, and the WS. We averaged the results from day 16 to day 20.

along-isobath PGF and enhance the wind-driven downslope transport (Gan et al. 2013; Pringle 2002), which could modulate the shelf dynamics and the CWCs. When we included the widened shelf in case topo_S, the elevation (and η_{x^*}) changed slightly (overlapping lines of case DW and case topo_S in Fig. 10a). The negative COR_{x^*}, induced by the enhanced downslope velocity, decreased the magnitude of the positive FORCE_{x^*} northeast of iGrid = 800 (not shown) and, thus, weakened the intensity of the CWC (the dashed orange line in Fig. 10b). Therefore, the widened shelf weakens the intensity of the CWC in the ECS but has a negligible effect in the Taiwan Strait and the NSCS.

2) TAIWAN ISLAND

In case topo_SI, the elevation rose south of iGrid = 680 (compared with case topo_S in Fig. 10a). The modulated η_{x^*} clearly demonstrated the influence of the Taiwan Island on the wind-induced elevation setup (with negligible influence on the density-induced η_{x^*}) over the shelf area on its shoreside (iGrid = 550–680) and over the shelf area further downstream (iGrid = 200–550). The enlarged η_{x^*} (or PGF_x^*) enhanced the intensity of the CWC between iGrid = 500–700 and turned the negative u^* between iGrid = 420–500 (Fig. 10b) to be positive. The significant increase in u^* between iGrid = 550 and iGrid = 680 was also partly due to the narrower shelf shoreside of the Taiwan Island (Fig. 2a). Yang (2007) suggested that the northward PGF within Taiwan Strait originates from the frictional effect of the Kuroshio flowing along the opposite side of Taiwan Island. Our study shows that, even without the strong western boundary current, Taiwan Island alone enlarged the magnitude of the wind-induced η_{x^*}, which enhanced the CWC intensity and extended its coverage further southward.

3) TAIWAN BANK

Taiwan Bank led to a local sea level elevation rise of about 0.05 cm (comparing case topo_SIB with case topo_SI), which strengthened (weakened) the positive PGF_{x^*} at the northern (southern) side. Taiwan Bank turned the local CWC toward the downwind direction. The change in direction occurred because the shallow water over the bank greatly strengthened the magnitude of the negative SSTR_{x^*} in the depth-mean momentum balance, overcoming the positive PGF_x^*. The elevation and u^* were not influenced by topography away from the bank. Li et al. (2018) and Shen et al. (2019) suggested that the blocking effect of Taiwan Bank would cause the southward flowing water to accumulate, which would generate the northward PGF and favored the formation of the CWC. Our study showed that, without the bank, there was still a northward PGF due to the alongshore variable wind and ATW effect. The elevation gradient induced by Taiwan Bank was limited, and the existence of the bank favored a southward current due to the enhanced wind stress effect.

4) HAINAN ISLAND

As in the case of Taiwan Bank, accumulating water due to the blocking by Hainan Island was regarded as an important contributor to the counterwind shelf current (Chao et al. 1995; Guan 1985). We investigated the influence of Hainan Island on the elevation in case topo_SIBH. Our results showed that the southward flow turned offshore as the flow approached Hainan Island (south of iGrid = 120, Fig. 9c). Thus, only a limited amount of water was accumulated near the island and slightly enhanced the positive η_{x^*} (PGF_{x^*}) locally (south of iGrid = 120, Fig. 10a). At the same time, the offshore flow also induced a negative COR_{x^*}, which partly offset the island-induced positive PGF_{x^*} and led to a slight change in FORCE_{x^*} (not shown), which weakened the southward current but was not sufficient to form a CWC. Thus, we found that Hainan Island was not a crucial factor in the formation of CWCs in the China shelf seas.

5) ALL THE TOPOGRAPHIC FEATURES

Figure 9c shows the flow pattern of case topo_SIBH, which included all the topographic features (the widened shelf, Taiwan Island, Taiwan Bank, and Hainan Island). Compared to case DW (Fig. 4c), the different topographies changed the overall pattern of the shelf currents only slightly. The southward current turned offshore as the current approached Hainan Island. Taiwan Bank favored the southward current and formed a clockwise circulation due to the enhanced wind's frictional effect. Taiwan Island enhanced the CWC intensity on the island's shoreside due to the strengthened alongshore elevation gradient and narrowing shelf width. The topographic features contributed to the more similar shelf current structures from the idealized model and the realistic simulations. The results from all the topographic cases show that the

topographic features of the China shelf seas are not critical to CWC formation, but they do influence the spatial structure of the currents.

5. Summary

We conducted a process-oriented idealized modeling study of the China shelf seas to investigate the fundamental dynamics of counterwind current (CWC) formation and to understand the spatiotemporal variations of CWCs in the region. In addition, our studies helped us to understand the influence of the different topographic features of the China shelf seas highlighted in previous studies. Our idealized model results reproduced the spatiotemporal characteristics seen in satellite observations and realistic simulations (Cheng and Gan 2025, manuscript submitted to *J. Geophys. Res. Oceans*) and isolated the dynamic processes involved in the formation of CWCs.

We found that the northward increasing density and northeasterly wind forcing jointly formed the southward increasing elevation over the China shelf seas. The alongshore elevation slope generated a northward pressure gradient force (PGF) and provided the potential forcing for the CWCs during the downwelling seasons. The alongshore varying density generated the alongshore current toward the dense water (northward in the China shelf seas) over the sloping shelf topography (Vennell and Malanotte-Rizzoli 1987). The wind set up northward alongshore PGF, offsetting part of the wind friction effect, but this PGF was still not enough for the CWC to form. However, the CWC appeared under the combined effects of the alongshore varying density and wind forcing. Wind forcing dominated the depth-mean momentum balance over the inner shelf (shoreward of the 50-m isobath) due to the shallow water depth and drove the southward current. Over the outer shelf (between the 50- and 100-m isobaths), the magnitudes of PGF_{x^*} and SSTR_{x^*} were comparable, and the balance among PGF_{x^*}, COR_{x^*}, and SSTR_{x^*} (or the direction of $\mathrm{FORCE}_{x^*} = \mathrm{PGF}_{x^*} + \mathrm{COR}_{x^*} + \mathrm{SSTR}_{x^*}$) determined the alongshore flow direction. Due to the negative baroclinic PGF_{x^*}, the magnitude of the density-induced total PGF_{x^*} was smaller compared to the wind-induced counterpart. However, it was critical for generating the positive FORCE_{x^*} term to form the CWC. Compared to the counterwind Leeuwin Current, which is caused by the steric effect (Godfrey and Ridgway 1985; McCreary et al. 1986; Morrow and Birol 1998), or the counterwind California Undercurrent (Connolly et al. 2014; Hickey and Pola 1983) caused by the coastal trapped wave-induced PGF, both alongshore varying density and wind are important for the CWCs in the China shelf seas.

Our results showed that the alongshore varying density and wind determined the spatiotemporal characteristics of the CWCs in the China shelf seas. During winter, the larger alongshore density gradient (favoring the CWC) in the northern part of the China shelf seas and stronger wind forcing (not favoring the CWC) in the southern part contributed to the CWC in the Taiwan Strait and the ECS but produced the southward current in the NSCS. During autumn, the weakened PGF_{x^*} (from wind and density effects) and weakened SSTR_{x^*} offset each other and led to a flow structure similar to what occurred during winter. The weakened wind intensity during spring was mainly why the CWC formed in the NSCS. Overall, the differences in the alongshore density and wind structure led to variations in the CWCs during different seasons.

We also examined the influences of different topographic features that included the widened ECS shelf, Taiwan Island, Taiwan Bank, and Hainan Island. We concluded that the combined effects of the alongshore variable wind forcing and density determined the fundamental CWC structure, and the different topographical features modulated the fundamental structure leading to a complicated small-scale structure, including the offshore turning flow near Hainan Island, southward flow over Taiwan Bank, and enhanced CWCs in the Taiwan Strait near the Taiwan Island side.

Our conceptual model provides a new understanding of the ambiguous CWC dynamics by including the vital forcing over the shelf. However, we realize that the China shelf seas is not an isolated system. The shelf currents are closely connected with intense slope dynamics (e.g., the mainstream of the Kuroshio in the ECS and the South China Sea branch of the Kuroshio), which are further linked with the dynamic processes in the China Seas and western Pacific Ocean. Chen and Yang (2024) found that the sub-Arctic inflow from the northern boundary made a significant contribution to the equatorward northwest Atlantic continental shelf current. For the China shelf seas, the along-shelf transport is weak at the southern (upstream of the CWC) end [<0.1 Sv ($1\ \mathrm{Sv} \equiv 10^6\ \mathrm{m^3\ s^{-1}}$), between Hainan Island and mainland China]. At the northern (downstream of the CWC) end, there is a ~1.8-Sv northeastward transport crossing the Tsushima Strait (Gan et al. 2016), which is partly induced by the CWC over the shelf, during the northeasterly monsoon season. Similarly, in this process-oriented study, we identify the intrinsic dynamics processes (i.e., internal wind-driven flow–topography interactions) that contribute to the CWC, and the outflux at the northern boundary should be the result of the intrinsically induced CWC in the China shelf seas rather than the sink–source dynamic proposed by Zheng et al. (2009). However, Lin et al. (2021) suggested that the spatial variation of the Kuroshio's intensity contributes to the alongshore elevation gradient in the China shelf seas. The relationship between coastal sea level elevation and a strong western boundary current (Gulf Stream) was also reported by Ezer et al. (2013) and Higginson et al. (2015). Therefore, in the future, our conceptual model should include open-ocean forcing to isolate oceanic contributions to the counterwind shelf currents in the China shelf seas.

Acknowledgments. The Hong Kong Research Grants Council GRF16307822, 16307423, 16310724, and AoE/P-601/23-N supported our research. CORE is a Joint Research Center for ocean research between Laoshan Lab and HKUST. We are also grateful for the support of the National Supercomputing Centers of Tianjin and Guangzhou. Thanks to the insightful comments from Dr. Jiayan Yang and anonymous reviewers, which improved the manuscript

Data availability statement. The data for this study are generated from the publicly distributed Regional Ocean Modeling System (ROMS; https://github.com/myroms/roms/releases, version 3.9). The model code; compilation script; model settings; topography, initial field, and wind forcing condition files; and data preprocessing codes and postprocessing codes are available at https://zenodo.org/records/17240710.

REFERENCES

Chao, S.-Y., P.-T. Shaw, and J. Wang, 1995: Wind relaxation as possible cause of the South China Sea Warm Current. *J. Oceanogr.*, **51**, 111–132, https://doi.org/10.1007/BF02235940.

Chen, K., and J. Yang, 2024: What drives the mean along-shelf flow in the northwest Atlantic Coastal Ocean? *J. Geophys. Res. Oceans*, **129**, e2024JC021079, https://doi.org/10.1029/2024JC021079.

Chiang, T.-L., C.-R. Wu, and S.-Y. Chao, 2008: Physical and geographical origins of the South China Sea Warm Current. *J. Geophys. Res.*, **113**, C08028, https://doi.org/10.1029/2008JC004794.

Chuang, W.-S., 1985: Dynamics of subtidal flow in the Taiwan Strait. *J. Oceanogr. Soc. Japan*, **41**, 65–72, https://doi.org/10.1007/BF02109175.

Connolly, T. P., B. M. Hickey, I. Shulman, and R. E. Thomson, 2014: Coastal trapped waves, alongshore pressure gradients, and the California undercurrent. *J. Phys. Oceanogr.*, **44**, 319–342, https://doi.org/10.1175/JPO-D-13-095.1.

Csanady, G. T., 1978: The arrested topographic wave. *J. Phys. Oceanogr.*, **8**, 47–62, https://doi.org/10.1175/1520-0485(1978)008<0047:TATW>2.0.CO;2.

——, 1981: Circulation in the coastal ocean. *Advances in Geophysics*, Vol. 23, Academic Press, 101–183, https://doi.org/10.1016/S0065-2687(08)60331-3.

Ezer, T., L. P. Atkinson, W. B. Corlett, and J. L. Blanco, 2013: Gulf Stream's induced sea level rise and variability along the U.S. mid-Atlantic coast. *J. Geophys. Res. Oceans*, **118**, 685–697, https://doi.org/10.1002/jgrc.20091.

Fang, G., and B. Zhao, 1988: A note on the main forcing of the northeastward flowing current off the Southeast China Coast. *Prog. Oceanogr.*, **21**, 363–372, https://doi.org/10.1016/0079-6611(88)90014-6.

——, ——, and Y. Zhu, 1991: Water volume transport through the Taiwan Strait and the continental skelf of the East China Sea measured with current meters. *Elsevier Oceanogr. Ser.*, **54**, 345–358, https://doi.org/10.1016/S0422-9894(08)70107-7.

Feng, X., M. N. Tsimplis, M. Marcos, F. M. Calafat, J. Zheng, G. Jordà, and P. Cipollini, 2015: Spatial and temporal variations of the seasonal sea level cycle in the northwest Pacific. *J. Geophys. Res. Oceans*, **120**, 7091–7112, https://doi.org/10.1002/2015JC011154.

Gan, J., and J. S. Allen, 2002: A modeling study of shelf circulation off northern California in the region of the Coastal Ocean Dynamics Experiment: Response to relaxation of upwelling winds. *J. Geophys. Res.*, **107**, 3123, https://doi.org/10.1029/2000JC000768.

——, H. San Ho, and L. Liang, 2013: Dynamics of intensified downwelling circulation over a widened shelf in the northeastern South China Sea. *J. Phys. Oceanogr.*, **43**, 80–94, https://doi.org/10.1175/JPO-D-12-02.1.

——, Z. Liu, and L. Liang, 2016: Numerical modeling of intrinsically and extrinsically forced seasonal circulation in the China Seas: A kinematic study. *J. Geophys. Res. Oceans*, **121**, 4697–4715, https://doi.org/10.1002/2016JC011800.

Gill, A. E., 1982: *Atmosphere–Ocean Dynamics.* Academic Press, 662 pp.

Godfrey, J. S., and K. R. Ridgway, 1985: The large-scale environment of the poleward-flowing Leeuwin Current, Western Australia: Longshore steric height gradients, wind stresses and geostrophic flow. *J. Phys. Oceanogr.*, **15**, 481–495, https://doi.org/10.1175/1520-0485(1985)015<0481:TLSEOT>2.0.CO;2.

Greatbatch, R. J., 1994: A note on the representation of steric sea level in models that conserve volume rather than mass. *J. Geophys. Res.*, **99**, 12 767–12 771, https://doi.org/10.1029/94JC00847.

Guan, B., and G. Fang, 2006: Winter counter-wind currents off the southeastern China coast: A review. *J. Oceanogr.*, **62**, 1–24, https://doi.org/10.1007/s10872-006-0028-8.

Guan, B. X., 1985: Some features of the temporal and spatial distributions of the 'counter-wind' current in northern South China Sea in winter (in Chinese). *Oceanol. Limnol. Sin.*, **16**, 429–438.

Helland-Hansen, B., 1934: The Sognefjord section: Oceanographic observations in the northernmost part of the North Sea and the southern part of the Norwegian Sea. *James Johnstone Memorial*, University Press of Liverpool, 257–274.

Hickey, B. M., and N. E. Pola, 1983: The seasonal alongshore pressure gradient on the West Coast of the United States. *J. Geophys. Res.*, **88**, 7623–7633, https://doi.org/10.1029/JC088iC12p07623.

Higginson, S., K. R. Thompson, P. L. Woodworth, and C. W. Hughes, 2015: The tilt of mean sea level along the east coast of North America. *Geophys. Res. Lett.*, **42**, 1471–1479, https://doi.org/10.1002/2015GL063186.

Hong, B., and D. Wang, 2006: Diagnostic analysis on the northern South China Sea winter counter-wind current. *Chin. Sci. Bull.*, **51**, 9–16, https://doi.org/10.1007/s11434-006-9009-y.

Kao, T. W., F.-S. Pan, and D. Renouard, 1985: Internal solitons on the pycnocline: Generation, propagation, and shoaling and breaking over a slope. *J. Fluid Mech.*, **159**, 19–53, https://doi.org/10.1017/S0022112085003081.

Laiz, I., L. Ferrer, T. A. Plomaritis, and G. Charria, 2014: Effect of river runoff on sea level from in-situ measurements and numerical models in the Bay of Biscay. *Deep-Sea Res. II*, **106**, 49–67, https://doi.org/10.1016/j.dsr2.2013.12.013.

Lentz, S. J., 2008: Observations and a model of the mean circulation over the Middle Atlantic Bight continental shelf. *J. Phys. Oceanogr.*, **38**, 1203–1221, https://doi.org/10.1175/2007JPO3768.1.

Li, L., X. Guo, E. Liao, and Y. Jiang, 2018: Subtidal variability in the Taiwan Strait induced by combined forcing of winter monsoon and topography. *Sci. China Earth Sci.*, **61**, 483–493, https://doi.org/10.1007/s11430-016-9132-9.

Lin, W., H. Lin, and J. Hu, 2021: The tilt of mean dynamic topography and its seasonality along the coast of the Chinese mainland. *J. Geophys. Res. Oceans*, **126**, e2020JC016778, https://doi.org/10.1029/2020JC016778.

Liu, Q., L. M. Rothstein, Y. Luo, D. S. Ullman, and D. L. Codiga, 2016: Dynamics of the periphery current in Rhode Island Sound. *Ocean Modell.*, **105**, 13–24, https://doi.org/10.1016/j.ocemod.2016.07.001.

McCreary, J. P., S. R. Shetye, and P. K. Kundu, 1986: Thermohaline forcing of eastern boundary currents: With application to the circulation off the west coast of Australia. *J. Mar. Res.*, **44**, 71–92, https://doi.org/10.1357/002224086788460184.

Morrow, R., and F. Birol, 1998: Variability in the southeast Indian Ocean from altimetry: Forcing mechanisms for the Leeuwin Current. *J. Geophys. Res.*, **103**, 18 529–18 544, https://doi.org/10.1029/98JC00783.

Pringle, J. M., 2002: Enhancement of wind-driven upwelling and downwelling by alongshore bathymetric variability. *J. Phys. Oceanogr.*, **32**, 3101–3112, https://doi.org/10.1175/1520-0485(2002)032<3101:EOWDUA>2.0.CO;2.

Qu, Y., S. Jevrejeva, J. Williams, and J. C. Moore, 2022: Drivers for seasonal variability in sea level around the China seas. *Global Planet. Change*, **213**, 103819, https://doi.org/10.1016/j.gloplacha.2022.103819.

Shchepetkin, A. F., and J. C. McWilliams, 2005: The regional oceanic modeling system (ROMS): A split-explicit, free-surface, topography-following-coordinate oceanic model. *Ocean Modell.*, **9**, 347–404, https://doi.org/10.1016/j.ocemod.2004.08.002.

Shen, J., and Coauthors, 2019: Winter counter-wind current in western Taiwan Strait: Characteristics and mechanisms. *Cont. Shelf Res.*, **172**, 1–11, https://doi.org/10.1016/j.csr.2018.11.005.

Swapna, P., J. P. Gan, A. Lau, and J. Fung, 2009: On the warm/cold regime shift in the South China Sea: Observation and modeling study. *Deep-Sea Res. I*, **56**, 1039–1056, https://doi.org/10.1016/j.dsr.2009.03.008.

Vennell, R., and P. Malanotte-Rizzoli, 1987: Coastal flows driven by alongshore density gradients. *J. Phys. Oceanogr.*, **17**, 821–827, https://doi.org/10.1175/1520-0485(1987)017<0821:CFDBAD>2.0.CO;2.

Wang, Q., Y. Wang, B. Hong, W. Zhou, and D. Wang, 2011: Different roles of Ekman pumping in the west and east segments of the South China Sea Warm Current. *Acta Oceanol. Sin.*, **30**, 1–13, https://doi.org/10.1007/s13131-011-0113-8.

Xu, F.-H., and L.-Y. Oey, 2011: The origin of along-shelf pressure gradient in the Middle Atlantic Bight. *J. Phys. Oceanogr.*, **41**, 1720–1740, https://doi.org/10.1175/2011JPO4589.1.

Yang, J., 2007: An oceanic current against the wind: How does Taiwan Island steer warm water into the East China Sea? *J. Phys. Oceanogr.*, **37**, 2563–2569, https://doi.org/10.1175/JPO3134.1.

Yu, Z., E. J. Metzger, and Y. Fan, 2021: Generation mechanism of the counter-wind South China Sea Warm Current in winter. *Ocean Modell.*, **167**, 101875, https://doi.org/10.1016/j.ocemod.2021.101875.

Zeng, Q., R. Li, Z. Ji, Z. Gan, and P. Ke, 1989: Calculation of monthly current in the South China Sea (in Chinese). *Sci. Atmos. Sin.*, **13**, 127–138.

Zhai, G. J., M. C. Zhao, and M. T. Huang, 1993: Computation and study of the SST in Chinese coastal waters. *Adv. Water Sci.*, **4**, 161–170.

Zhang, C., Y. Ding, X. Bao, C. Bi, R. Li, C. Zhang, B. Shen, and K. Wan, 2018: A numerical study of the South China Sea Warm Current during winter monsoon relaxation. *J. Oceanol. Limnol.*, **36**, 216–229, https://doi.org/10.1007/s00343-018-6302-y.

Zhang, C. J., 2002: The sea level slope along China's Coast of the northwest Pacific and its primary research on mechanism. *Acta Oceanol. Sin.*, **24**, 19–25.

Zheng, P.-n., D.-x. Wu, and X.-p. Lin, 2009: The relationship between the Taiwan Warm Current and Tsushima Warm Current. *J. Hydrodyn.*, **21**, 212–218, https://doi.org/10.1016/S1001-6058(08)60138-9.